Journal of the Optical Society of America B
OPTICAL PHYSICS

Imaging properties of surface-enhanced coherent anti-Stokes Raman scattering microscopy on thin gold films

John P. Kenison,[1] Alexander Fast,[2] Facheng Guo,[2] Alexander LeBon,[2] Wei Jiang,[3] and Eric O. Potma[2,*]

[1]Department of Physics and Astronomy, University of California, Irvine, California 92697, USA
[2]Department of Chemistry, University of California, Irvine, California 92697, USA
[3]Environment Research Institute, Shandong University, Jinan 250100, China
*Corresponding author: epotma@uci.edu

Received 19 June 2017; revised 20 August 2017; accepted 21 August 2017; posted 22 August 2017 (Doc. ID 300378); published 12 September 2017

In a wide-field surface-enhanced coherent anti-Stokes Raman scattering (SE-CARS) microscope, the sample is driven by surface plasmon polaritons supported on a thin gold film. Subsequent radiation at the anti-Stokes frequency is coupled through the gold layer onto a far-field camera, enabling the recording of surface-enhanced CARS images of structures in close proximity to the gold surface. The effective enhancement of the CARS signal can be as high as seven orders of magnitude, allowing CARS imaging at extraordinarily low light levels. In this work, we analyze the imaging properties of the SE-CARS microscope in detail, which are markedly different from the imaging properties of a point-scanning CARS microscope. Using a dipole model to describe the sample, we show that the strength of the signal and the appearance of coherent artifacts depend strongly on the geometry of the sample. We explain the observed radiation profile in the back focal plane and discuss representative imaging examples. © 2017 Optical Society of America

OCIS codes: (180.4315) Nonlinear microscopy; (190.4380) Nonlinear optics, four-wave mixing; (190.4710) Optical nonlinearities in organic materials; (190.5650) Raman effect.

https://doi.org/10.1364/JOSAB.34.002104

1. INTRODUCTION

Although the Raman effect is a weak light–matter interaction, strong signals can nonetheless be generated with the help of the enhanced optical properties of nanostructured metals [1,2]. The concentration of the excitation field and the enhancement of radiative rates mediated by the metal's plasmonic modes can raise the otherwise imperceptible Raman signal from single molecules to detectable levels [3–5]. The amplifying qualities of metallic nanostructures are ideally suited for detecting and identifying molecular species at low concentration, spurring the development of chemical sensors based on surface-enhanced Raman scattering (SERS) into a burgeoning field. The principle of SERS, however, has not yet been successfully translated to improved Raman imaging and microscopy. Because the optical enhancement in SERS substrates is confined to nano-sized hot-spots, signal amplification is generally not uniform across the entire field of view, rendering this approach unsuitable for detailed imaging applications [6].

To achieve a uniform amplification of optical signals, flat metal films can be used as the plasmonic material. Compared to the localized surface plasmon modes utilized in most SERS substrates, the optical enhancement at flat films is facilitated by surface plasmon polariton (SPP) excitations, which generally offer a lower field enhancement but provide amplifying qualities that are constant within the two-dimensional sample plane. SPP-based Raman spectroscopy has been used in various sensor applications [7–10], and has also been employed to boost the signals in the imaging mode [11]. For instance, the SPP-Raman microscope has been used to visualize micro-structured films of organic materials [12]. The application of SPP-based Raman microscopy to biological samples remains, however, a challenge. To raise the weak Raman signals from the endogenous compounds in biological specimens, further amplification is desired. The latter can be achieved, in principle, by combining SPP excitations with coherent Raman scattering (CRS) microscopy.

In CRS, the molecules are coherently driven by the excitation fields, yielding coherent signals in a phase-matched direction. The CRS signals from ensembles of molecules are generally much stronger than what can be obtained in spontaneous Raman scattering. This principle has been used efficiently in laser-scanning CRS microscopy, which enables Raman-sensitive imaging at speeds that exceed 1 frame/second

[13–15]. The combination of CRS with surface enhancement has a long history, including early SPP-mediated coherent anti-Stokes Raman scattering (CARS) studies [16] and recent demonstrations of surface-enhanced CARS (SE-CARS) of single molecules using dedicated plasmonic nanoantennas [17–19].

The success of laser-scanning CRS on one hand, and surface-enhanced CRS on the other, suggests the feasibility of SPP-based coherent Raman microscopy. Indeed, recent studies have shown that SE-CARS images of lipid droplets can be generated in the wide-field imaging mode using a gold film as the plasmonic material [20]. The amplifying properties of the gold film were found to be sufficient to produce images at rates that are comparable to laser-scanning CRS microscopy. These developments insinuate that surface-enhanced CARS microscopy of cells is possible, offering a route to examine the cortical regions of cells that are within the evanescent reach of the gold substrate. However, compared to the incoherent SPP-Raman microscope, the imaging properties of the SPP-CARS microscope are markedly more complex. For instance, the gold substrate itself exhibits strong nonlinear properties, including an electronic four-wave mixing response, that may overwhelm the Raman resonant signal from the sample. In addition, the coherent radiation from the driven Raman oscillators in the sample plane produces interference in the image plane that may complicate the image analysis. Before SPP-based CARS microscopy can be applied to study biological samples, a better understanding of the imaging properties of the wide-field SE-CARS microscope is required.

In this work, we present a theoretical and experimental analysis of a wide-field, SPP-based CARS imaging system. To better understand the different contributions to the nonlinear signal, we study the signal in the image plane as well as in the back focal plane (BFP) of the microscope objective. We identify signal contributions from both the sample and the gold substrate, and show that multiphoton fluorescence can be conveniently distinguished from the coherent nonlinear signal in the BFP. Using a simple dipole radiation model, we rationalize the origin of the observed artifacts in the SE-CARS images. Finally, we discuss the merits of the SPP-CARS microscopy technique and point to future applications of this method in biological imaging.

2. MATERIALS AND METHODS

A. Microscope Setup

A schematic of the wide-field SE-CARS microscope is shown in Fig. 1. The system uses two input beams, a pump and a Stokes beam, to drive the CARS process. Both beams are derived from a light source that consists of a pump laser and a synchronously pumped optical parametric oscillator (OPO). The pump laser is a Nd:vanadate oscillator (PicoTrain, High-Q) that produces 7 ps pulses at a center wavelength of 1064 nm. A portion of the laser output is used as the Stokes beam in the CARS process. Another portion of the output is frequency doubled and used to synchronously pump the OPO (Levante Emerald, APE-Berlin). The OPO delivers tunable radiation in the 780–920 nm range. For the CARS experiments discussed here, the OPO wavelength is set in the range from 800 to 825 nm, producing the pump radiation for the CARS process. The Raman shift in this study is

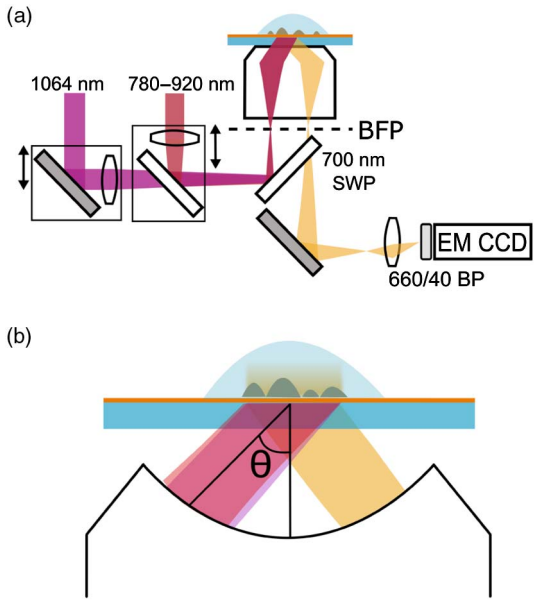

Fig. 1. Sketch of the wide-field surface-enhanced CARS microscope. (a) The Stokes (1064 nm) and pump (tunable) beams are independently focused onto the bBFP of the objective lens. Radiation from the sample plane is projected onto an imaging EM-CCD camera. (b) The collimated Stokes and pump beams are incident onto the gold-coated coverslip at their respective Kretchmann angles.

tuned to the 2700–3000 cm^{-1} spectral range corresponding to the energy of the C-H vibrational stretching modes.

The pump and Stokes beams are separately conditioned with spatial filters and expanded to a ~7 mm beam diameter. Both beams exhibit linearly polarized Gaussian transverse profiles. The beams are independently focused onto the BFP of a 60× 1.49 NA oil immersion objective (APON60XOTIRF, Olympus) to achieve wide-field illumination. The alignment allows for an angular difference between the beams as dictated by the different plasmon coupling angles of the pump ($\theta_{pump} = 65.1°$) and Stokes ($\theta_{Stokes} = 63.1°$) beams.

For each beam, a 25 mm effective focal length (EFL) plano–concave and 75 mm EFL plano–convex lens expands and then focuses the radiation onto the BFP of the objective. Each lens combination is mounted to a translation stage, allowing independent adjustment of the lateral position of the focused spots on the BFP. The beams are quasi-collinearly overlapped in time and space with a 50/50 beam splitter that is placed after the focusing lenses of the beams. The coupling efficiency to propagate SPP modes is determined experimentally by monitoring the reflectivity changes from the gold film. The lower reflectivity from the gold layer corresponds to greater energy coupling into the SPP mode. The CARS radiation is detected in the epi-direction and separated from the incident light by a dichroic mirror (Semrock SWP 700 nm). Radiation from the sample plane is projected onto an imaging EM-CCD (Andor iXon) camera using two bandpass filters (Chroma ET660/40) to isolate the CARS signal. In the case of BFP imaging, a Bertrand lens is inserted in the detection path to project the BFP onto the EM-CCD camera sensor.

The average power at the sample is ~60 mW per beam for the entire field of view (FOV), corresponding to less than

10 μW per μm^2. Images are taken with a 1 s integration time in the electron multiplication acquisition mode.

B. Sample Preparation

Sample substrates consist of borosilicate glass coverslips (BK-7, VWR) coated with gold. The coverslips are first pre-treated with a 2 nm Cr adhesion layer. Then, gold thin films are evaporated to a thickness of 30 nm on the coverslips. For patterned Au films, lithographic masks are used for depositing S1808 photoresist (Shipley) onto the surface, followed by chemical etching.

The lipid samples used in the experiments are droplets and crystals of cholesteryl oleate (Sigma Aldrich). The droplets are formed by preparing an emulsion of cholesteryl oleate with phosphatidylcholine in phosphate-buffered saline (PBS). Using ~50 μL of a stock solution, the emulsion is subsequently spin coated on the Au-covered microscope coverslips, resulting in air-dried droplets and micrometer-sized polymorphous crystals of cholesteryl oleate on the surface. We use a coumarin dye (coumarin 521T, TCI) as a generic two-photon excitable fluorophore. The dye is prepared as a 1 mM solution in water. Giant unilamellar vesciles (GUVs) are prepared from 1,2-dioleoyl-sn-glycero-3-phosphocholine (DOPC) and 10% 1,2-dioleoyl-3-trimethylammonium-propane (DOTAP), and are suspended in water.

C. Simulation Details

The simulated configuration consists of an upper half-space filled with water, characterized by a (real) permittivity ε_1, and a lower half-space of glass with permittivity ε_3. We assume that the permeabilities of each of the half-spaces can be set to $\mu = 1$. The two hemispheres are separated by a thin gold layer (30 nm), with permittivity ε_2, as shown in Fig. 2. Excitation fields are simulated as monochromatic SPP surface waves at the pump (p) and Stokes (s) frequencies [21]:

$$\mathbf{E}(\omega_u) = \begin{bmatrix} 1 \\ 0 \\ -k_{u,x}/k_{u,z} \end{bmatrix} e^{i(k_{u,x}x + k_{u,z}z)}, \tag{1}$$

where $u = p, s$. The field is evanescent in the z direction, and propagation of the SPP mode is along the x direction with a wave vector $k_{u,x}$. We will indicate the propagating mode with the wave vector k^{spp}, which is related to the free-space excitation field (vacuum) wave vector k_0 as

$$k^{\mathrm{spp}} = k_0 n_3 \sin\theta_{\mathrm{spp}}, \tag{2}$$

where

$$\theta_{\mathrm{spp}} = \sin^{-1}\left\{\frac{1}{n_3}\sqrt{\frac{\varepsilon_1\varepsilon_2'}{\varepsilon_1 + \varepsilon_2'}}\right\}. \tag{3}$$

Here ε_2' is the real part of ε_2. The angle θ_{spp} is referred to as the plasmon coupling angle, which in this configuration is also known as the Kretschmann angle for the incident field. The surface fields $\mathbf{E}(\omega_p)$ and $\mathbf{E}(\omega_s)$ induce a third-order polarization in the material in the upper half-space. In this work, we use a dipole model to describe the material response, which assumes that the material can be modeled as a collection of nonlinearly induced dipoles [22,23]. The components of the nonlinear polarization $\mathbf{p}^{(3)}(\omega_{\mathrm{as}})$ of a dipole oscillator placed at position $\mathbf{r}$ in the upper half-space is given as

$$p_i^{(3)}(\omega_{\mathrm{as}}, \mathbf{r}) = \gamma_{ijkl}(\omega_{\mathrm{as}}, \mathbf{r}) E_j(\omega_p, \mathbf{r}) E_k(\omega_p, \mathbf{r}) E_l^*(\omega_s, \mathbf{r}), \tag{4}$$

where $\omega_{\mathrm{as}} = 2\omega_p - \omega_s$ is the anti-Stokes frequency and γ_{ijkl} is the third-order hyperpolarizability of the dipole at location $\mathbf{r}$. The hyperpolarizability is a tensor, but for simplicity we assume that it only has nonzero diagonal elements and that the response is isotropic. For clarity, we assume that the non-resonant response from the water medium can be ignored ($\chi^{(3)}_{\mathrm{water}} \approx 0$), so that the radiative properties of the CARS-active dipoles that make up the target structure can be studied in detail. Using an 817 nm pump beam and a 1064 nm Stokes beam, the anti-Stokes radiation is found at 663 nm, where the permittivity of gold is $\varepsilon_2 = -13.883 + 1.038i$ [24].

The far-field radiation at ω_{as} is collected in the lower half-space at the points R on a hemispherical surface. The transmission through the gold layer requires modeling of a planar, layered medium. For this purpose, we use an asymptotic far-field Green's function for layered media, where the gold layer is described by generalized Fresnel coefficients. The far-field contribution of a dipole radiator at point $\mathbf{r}$ to the field detected at point $\mathbf{R}$ is [21]

$$\mathbf{E}_d(\mathbf{R}) = \frac{\omega^2}{\epsilon_0 c^2}\overline{G}(\mathbf{R}, \mathbf{r})\mathbf{p}^{(3)}, \tag{5}$$

where $\overline{G}$ is the far-field Green's function. Details on the Green's function are found in Appendix A. The total CARS field in point $\mathbf{R}$ is the sum of the contributions from each of the dipole emitters in the upper half-space:

$$\mathbf{E}(\mathbf{R}) = \frac{\omega^2}{\epsilon_0 c^2}\int \mathrm{d}V \overline{G}(\mathbf{R}, \mathbf{r})\mathbf{p}^{(3)}, \tag{6}$$

where the integration is over the volume V of the upper half-space. For the CARS process, which is coherent, the intensity at point $\mathbf{R}$ is directly proportional to the square modulus of the summed field, i.e., $I(\mathbf{R}) \propto |\mathbf{E}(\mathbf{R})|^2$. If the radiation is incoherent, as is the case for the multiphoton excited fluorescence background, the intensity is written as $I(\mathbf{R}) \propto \int \mathrm{d}V |\mathbf{E}_d(\mathbf{R})|^2$, where the dipole radiation now results from a nonlinearly excited fluorescence process. For better visualization, the field distribution on the hemisphere is projected to a planar

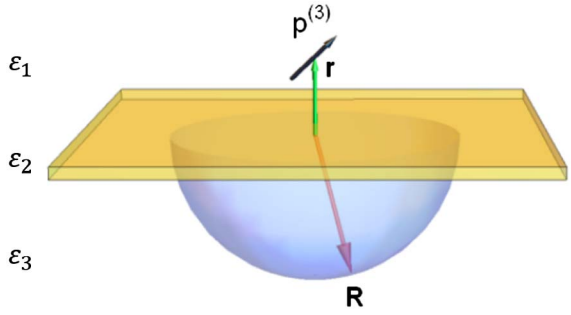

Fig. 2. Schematic of the simulated configuration. A dipole positioned at $\mathbf{r}$ is located in the space above the gold layer. Radiation of the dipole is collected through the gold layer in the glass medium on the surface of the lower far-field hemisphere (radius = 1 m).

two-dimensional surface, which represents the image in the BFP. A Fourier transform of the BFP image provides a representation of the sample plane image in the far field.

3. RESULTS

A. Incoherent Contributions: Two-Photon Excited Fluorescence

We first study the contributions from fluorescent species that are tentatively excited in a typical wide-field SE-CARS experiment through a two-photon excitation process and thus give rise to an incoherent background signal. While we observe induced two-photon excited fluorescence (TPEF) from both the pump and Stokes beams, the strongest contribution is observed from the pump beam. For this reason, we focus here on TPEF generated by the pump beam set to 817 nm, while blocking the Stokes beam. Under these conditions, no SE-CARS signal is observed, and the signal that is detected through the CARS bandpass filter originates from the pump-induced TPEF process.

There are two main contributions to the TPEF background: (1) emission from fluorescent compounds that are present in the sample, and (2) TPEF from the gold layer. If the sample contains fluorophores with a high quantum yield at high concentration, then the observed image on the CCD camera is dominated by the sample fluorescence. An example is shown in Fig. 3, where clusters of coumarin dye close to the surface are visualized. This imaging mode shares similarity with total internal reflection fluorescence (TIRF) microscopy [25,26], with the important difference that here the evanescent field is provided by the SPP mode. Surface-enhanced TPEF with SPP modes has been suggested as a tool to enhance the efficiency of TIRF [27]; however, suitable spacers are required to suppress quenching of the fluorophores that are proximal to the metal film [28].

In Fig. 4(a), we examine the TPEF in the BFP of the objective lens. The incoherent fluorescence appears as a thin, symmetric ring corresponding to the Kretschmann coupling angle of the emitted radiation. This pattern is expected for surface plasmon mediated emission of dipoles in the upper half

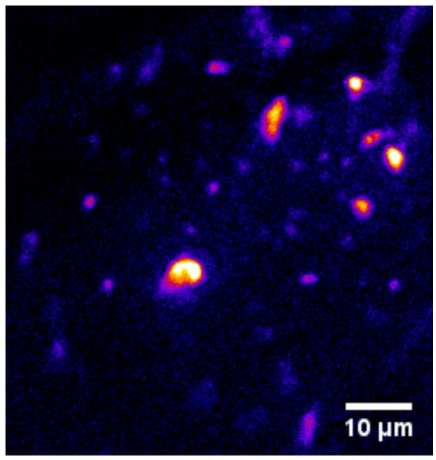

Fig. 3. Wide-field TPEF image obtained from clusters of coumarin dye on the gold layer in water. Fluorescence is induced by the 817 nm pump beam.

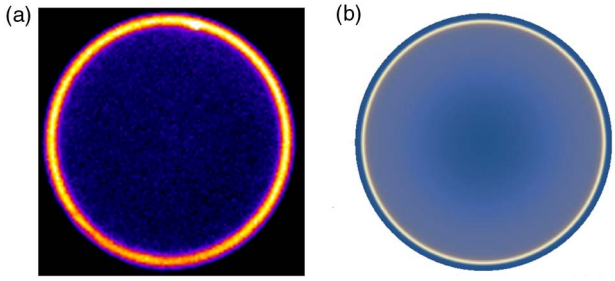

Fig. 4. TPEF observed in the BFP. (a) The experiment using coumarin in water. (b) The simulation based on a random distribution of incoherent dipole emitters placed in the sample plane, 1 nm above the gold film. The BFP pattern in this case is independent of the dipole placement and resembles that of a single coherent dipole emitter.

sphere [29]. In Fig. 4(b), a simulation of the incoherent dipole emission is shown, confirming the pattern that is observed experimentally.

If the sample is devoid of fluorophores, a weak emission can sometimes still be observed. For instance, when non-fluorescent lipid droplets or polystyrene beads are placed on the gold surface, TPEF can be seen from the location of the object. This fluorescence results from the two-photon induced inter-band transition in gold, followed by radiative emission upon electron-hole recombination [30]. This contribution is virtually undetectable in the case of bare gold film, but is enhanced when objects are placed on the surface, suggesting that local field effects may enhance the coupling of radiation to the far field. Hence, enhanced local fields at the nanoscopic junctions between dielectric particles and the gold film provide imaging contrast through locally enhanced gold TPEF at the particle's location. Much higher contrast is observed for dry-mounted objects compared to the case when the sample is immersed in water. The gold-related TPEF also appears as a ring-like structure in the BFP, identical to sample fluorescence. In some cases, the TPEF from gold rivals the SE-CARS signal, forming an unwanted background. A straightforward way to suppress the fluorescence is to collect images with (I_{Total}) and without (I_{TPEF}) the Stokes beam, and retrieve the CARS image by computing the normalized difference:

$$I_{\mathrm{CARS}} = \frac{I_{\mathrm{Total}} - I_{\mathrm{TPEF}}}{I_{\mathrm{TPEF}}}. \tag{7}$$

Alternatively, the unique distribution of the TPEF in the BFP also offers an opportunity to discriminate the incoherent fluorescence from the CARS signal, as the emission characteristics are different. In the next sections, we discuss the characteristics of coherent radiation in the image plane and in the BFP.

B. Coherent Contributions: Surface-Enhanced CARS

We next examine the SE-CARS signal by coupling both the pump and Stokes beams to SPP modes. Without a Raman active sample, the signal from the bare gold film is negligible. This indicates that intrinsic four-wave mixing (FWM) in the gold or at the gold interfaces is not contributing to a noticeable background in the absence of a sample. Strong coherent radiation

can be clearly observed, however, if lipid droplets are placed on the surface. The detected signal scales quadratically with the pump beam and linearly with the Stokes beam, as shown in Fig. 5(a). The signal peaks whenever the pump and Stokes beams overlap in time, as is evident in Fig. 5(b). At longer time delays, no coherent signal is observed, and the detected signal at these settings is governed by TPEF induced by the individual excitation beams.

These observations confirm that the coherent signal originates from a four-wave mixing process, producing a signal at ω_{as}. This signal can have both vibrational and electronic contributions. In Fig. 6 we investigate the dependence of the signal on the Raman shift in the 2800–2950 cm^{-1} vibrational energy range. The sample consists of a GUV of DOPC, shown in the SE-CARS image in Fig. 6(c). The spectrum of the vesicle is derived from the single bilayer that contacts the surface. This spectrum is represented by the red squares in Fig. 6, yielding a CARS line shape that is typical for phospholipids [31,32]. For comparison, we collected a CARS spectrum in laser-scanning mode (i.e., regular CARS microscopy) from a multilamellar particle of the same DOPC material, indicated by the black circles in Fig. 6(a). Note that, unlike the GUV in the SE-CARS image, this particle is composed of multiple membranes folded into an amorphous structure. The spectra appear very similar, thus confirming the presence of a vibrational CARS contribution in SE-CARS. However, the spectra are not totally identical. This suggests that mixing contributions from electronic FWM are somewhat different between the two imaging modes. Indeed, similar to enhanced TPEF from gold in areas where

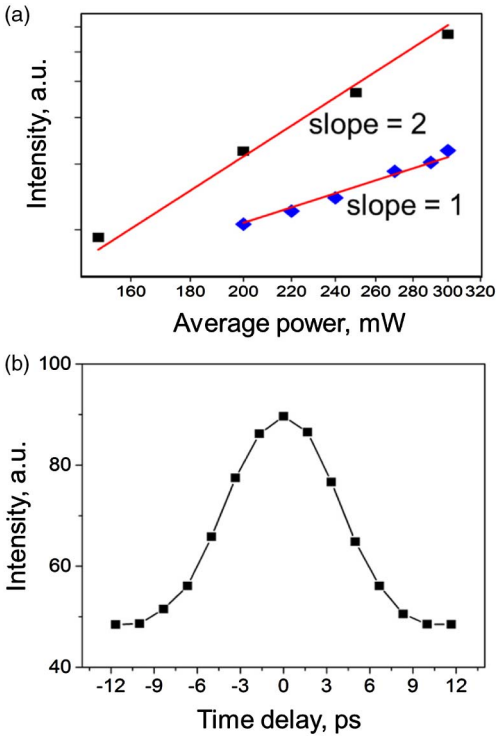

Fig. 5. Characteristics of the observed signal. (a) The power dependence of the pump (black squares) and Stokes (blue diamonds) beams. (b) The dependence of the observed signal as a function of the pulse overlap in time.

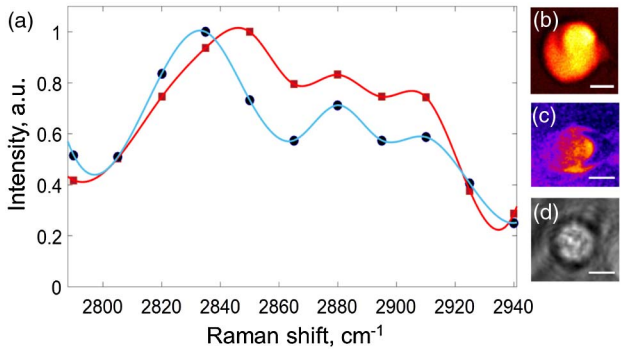

Fig. 6. Spectral dependence of the surface-enhanced CARS signal. (a) A comparison of the CARS spectrum of the lipid collected in the wide-field, surface-enhanced configuration (red squares) and in the laser-scanning configuration (blue circles). (b) The multilamellar vesicle of DOPC on glass visualized at 2845 cm^{-1} in the laser-scanning imaging mode. (c) The GUV on the gold surface recorded at 2845 cm^{-1} in wide-field SE-CARS mode. (d) The transmission image of the GUV shown in (c). The scale bar is 5 μm.

the samples contact the metal surface, there is enhanced FWM from the gold near the contact regions [20]. Therefore, the non-resonant contributions in wide-field SE-CARS are generally higher than what is commonly seen in laser-scanning CARS microscopy. Moreover, the magnitude of the gold FWM contribution is dependent on the sample material, the morphology of the object, and the structural details in the contact region. These factors introduce small variations in the amount of the electronic FWM signal that is mixed in with the vibrational CARS signal. Nonetheless, as is evident from Fig. 6, the vibrational contrast is clearly seen, thus allowing vibrational imaging in SE-CARS mode with confidence. We note that, for the power levels used in the experiments described here, the observed CARS signal is only visible when the gold layer is present. When a bare glass surface is used, no CARS signal is detected [20].

C. Characteristics of Coherent Radiation

In the previous sections, we established that the detected signal in SPP-based CARS imaging contains a clear vibrational CARS signal in addition to weak contributions from enhanced FWM and TPEF from gold/sample contact regions. In this section, we study the radiation characteristics of the coherent CARS contributions and how the radiating field produces certain image features in the far field. We have already seen in Section 3.A that the incoherent TPEF is distributed in a ring-like distribution in the BFP due to the radiative coupling through gold film. Here we discuss the coherent radiation of dipoles placed near the gold surface using the Green's function formalism outlined in Section 2.C, followed by a comparison with experiment.

The evanescent SPP excitation fields given in Eq. (1) contain both x and z polarization components. Since there is a $\pi/2$ phase shift between E^x and E^z, the dipole is effectively driven by an elliptical excitation field. In our example of an isotropic induced dipole, radiative components of both x and z can be expected. Since $E^z > E^x$, the z polarized component is expected to be the dominant contribution at the far-field detector,

and the sample effectively behaves as a collection of vertically oriented dipole emitters.

Figure 7 shows the angularly resolved CARS radiation from a dipole near the gold film, as observed in the lower half-space. In Fig. 7(a), the dipole is positioned close to the gold surface at a distance of 1 nm. At this proximal distance, coupling through the film is very efficient, resulting in a ring-like distribution of the radiation in the BFP. This situation is very similar to linearly excited dipoles close to the surface [29,33,34], where the radiation is highly confined to angular components close to the plasmon coupling angle, resulting in an azimuthally symmetric radiation pattern. The angle of maximum emission intensity $\theta_{sp} = 69.6°$ lies above the critical angle $\theta_c = 61°$, which partitions the signal into contributions from plane waves below θ_c and coupled evanescent light above θ_c [35–37]. The former being associated with direct dipole emission through the film and the latter coming from optical tunneling and leakage radiation of the evanescent fields originating from excited SPP fields at ω_{as}. For the geometry relevant here, the propagation length of the SPP mode excited at the anti-Stokes frequency is $L_{spp} = 13$ μm [38,39]. These propagating surface wave contributions to the signal give rise to distinct imaging artifacts, as will be discussed below.

In Fig. 7(b), the dipole is placed farther away from the gold surface, at a distance of 250 nm. The radiation pattern shows some markedly different features in the BFP. Portions of evanescent contributions can still be seen beyond θ_c, but the narrow ring of k vector components that originated from SPP-coupled radiation is now much weaker. In Fig. 7(c), the dipole is placed 1 μm away from the surface. At these distances, no evanescent contributions are passed through the film and the remaining radiation originates from direct (far-field) dipole emission through the film. This example underlines that, depending on the distance of the dipole from the surface, different radiative contributions can be expected. In particular, for dipoles within a few nm from the surface, the SPP-coupled radiation is strong, a contribution that disappears for dipoles that are situated farther from the surface.

The dipole radiation pattern is shown again in Fig. 8(a), as seen in the BFP. Figure 8(b) shows the radiation pattern resulting from a collection of dipoles that are aligned in the y direction, perpendicular to the direction of propagation of the surface excitation fields. Whereas the ring-like structure can still be recognized, there are clear interferences observed between the ω_{as} radiation of the individual dipoles. The pattern reflects the destructive and constructive interference of the dipole radiators in the y direction, while their contributions remain in-phase along the x axis, producing bright portions of radiation in this direction The pattern changes dramatically when the point dipoles are arranged along x, as depicted in Fig. 8(c). No interferences are observed in the y direction, while the mutual spacing between the emitters along x gives rise to maxima and minima. In addition, the signal is significantly stronger on one side of the radiation cone. The stronger signal reflects the fact that the dipoles radiate in phase in this direction due to phase matching between the excitation fields and the anti-Stokes emitted field. The coherence length, given as $L = \pi/(2k_p^{spp} - k_s^{spp} - k_{as}^{spp})$, is longer than 10 μm. Since L is on the order of the SPP propagation length, the SPP wave has the opportunity to grow during its propagation due to constructive interference along the x direction.

In Fig. 8(d) we show the CARS radiation pattern from a collection of dipoles that are organized in a square array. The size of the square exceeds the wavelength λ_{as}^{spp} of the anti-Stokes radiation by several times, and we may thus expect a highly directional signal that is in phase predominantly along the direction of k_x^{spp} [34]. Indeed, because of phase matching, the azimuthal distribution in the BFP is broken and the signal now peaks exclusively in one direction. The amount of light coming from the phase-matched direction is over an order of magnitude higher than from a similar area on the ring. Note that such a radiation pattern is radically different from the BFP signal distribution for incoherent emission. In the latter case, the signal always exhibits azimuthal symmetry,

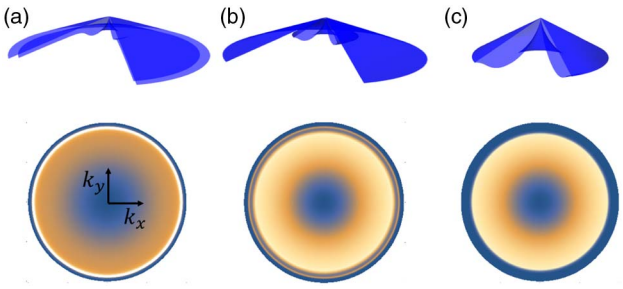

Fig. 7. Simulated CARS radiation of a driven dipole emitter into the lower half-space as a function of height above the interface. The intensities are rescaled in each case to highlight features in the emission pattern. (a) A dipole placed 1 nm above the gold surface. (b) A dipole placed 250 nm above the gold surface. (c) A dipole placed 1000 nm above the gold surface.

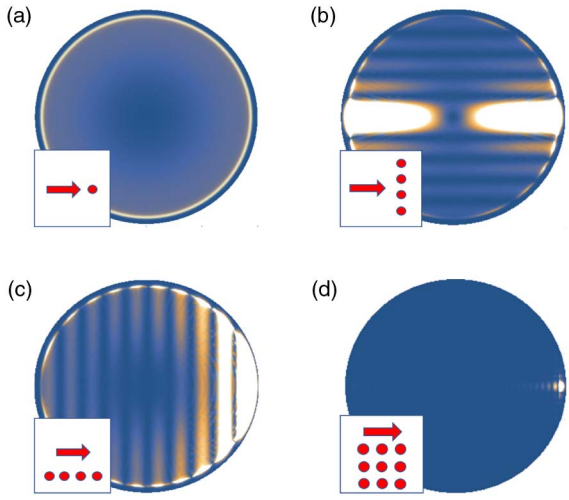

Fig. 8. CARS radiation patterns from dipole emitters in the BFP. (a) A ssingle dipole 1 nm above the gold interface. (b) A dipole chain of 16 dipoles spaced 150 nm apart at a height of 1 nm above the gold layer, aligned perpendicular to the propagation direction. (c) A dipole chain of 16 dipoles spaced 150 nm apart at a height of 1 nm above the gold layer, aligned in the direction of propagation. (d) A 50×50 square array of dipoles 1 nm above the gold layer. The arrow indicates the direction of propagation of the surface excitation fields.

independent of the positioning of the emitting dipoles in the sample plane.

The discussion above suggests that CARS and TPEF radiation appear differently in the BFP. Figure 9 shows an experimental realization of this notion. In Fig. 9(a), several clusters of cholesterol oleate deposited on the gold surface form a CARS signal at 2845 cm^{-1}, which is visualized in the BFP. The image shows the familiar azimuthal pattern of the signal in addition to a clear bright spot near the k_x^{spp} location. Note that the intensity of the phase-matched radiation spot is saturated in the figure to make the annular incoherent contribution visible. The image in Fig. 9(b) is observed when the pump and Stokes beams are temporally detuned. This generates an image similar to Fig. 9(a) but without the bright spot. We may thus conclude that the signal along the ring shown in Fig. 9(b) is due to TPEF of the gold film, whereas the additional bright spot is due exclusively to the phase-matched CARS signal. This comparison also underlines the feasibility of using masks in the BFP to suppress the TPEF contributions while passing the CARS portion of the signal.

We next study the SE-CARS signal from two structures in the image plane. Figure 10(a) depicts the simulated SE-CARS image of an array of point dipoles arranged along the x direction. The linear alignment of the dipoles is clearly distinguished in the image. However, the excitation of SPP waves by each of the dipoles gives rise to SPP leakage radiation at ω_{as} over a length scale corresponding to L_{spp}. As discussed above, efficient excitation of SPP waves is expected when the point dipoles are within several nm of the gold surface. Because the individual SPP contributions are in phase in the positive x direction, the image contains a directional, flare-like feature that appears to emanate from the dipole chain. In the negative x direction, the SPP waves are not in phase, resulting in a depleted signal at the other end of the chain structure. A similar observation is made in Fig. 10(b), which depicts the SE-CARS image of dipoles organized in a 3 μm diameter ring. The ring structure is reproduced in the CARS image, along with the directional SPP leakage radiation. The positions of the radiating dipoles is such that additional interference can be seen in the flare that stretches along the positive x direction. We note that the flaring effect is suppressed for point dipoles that are spaced farther away from the surface. These examples show that SE-CARS images contain coherent features that are absent in incoherent TPEF images.

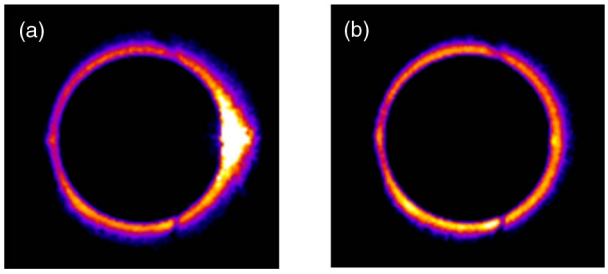

Fig. 9. SE-CARS imaging in the BFP. (a) A BFP image of clusters of cholesteryl oleate on the gold surface at 2845 cm^{-1}. (b) A BFP image of the same sample when the pump and Stokes pulses are temporally detuned.

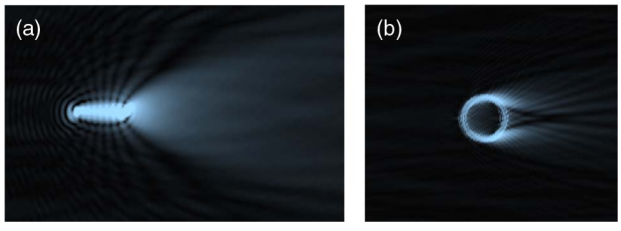

Fig. 10. (a) Simulated chain of 32 dipoles spaced 150 nm apart. (b) A simulated image of a 3 μm diameter ring made up of dipoles spaced 150 nm apart. In both cases, the dipoles are placed 1 nm away from the gold surface. The field values are recorded on a 1 m radius glass hemisphere in the lower half-space and Fourier transformed to produce a real-space image.

D. SE-CARS Imaging Examples

Figure 11(a) shows an SE-CARS image of cholesteryl oleate droplets deposited on the gold surface. Because the thickness of the droplets exceeds the penetration depth of the CARS excitation field (~100 nm), the signal originates only from cholesteryl oleate that falls within the evanescent excitation volume [20]. The image is not affected by interference from SPP-related flares, because the ω_{as} radiation of only a relatively small portion of the driven molecules is efficiently coupled to the SPP mode. When the Stokes beam is blocked, the SE-CARS signal disappears and the remaining TPEF signal becomes clearly visible, as shown in Fig. 11(b). Recall that the TPEF emission results from the gold and is thus not necessarily sensitive to the chemical composition of the objects themselves.

The SE-CARS images from thinner structures look noticeably different. An example of a thin structure is found in the GUV image in Fig. 6(c). Because the phospholipid molecules are close to the gold surface, coupling to an SPP mode at ω_{as} is efficient, producing clear streaks in the image. The dark spot found on one end of the structure is reproduced in the simulation of Fig. 10(b). This example confirms that the morphology of the structure plays an important role in the amount of flaring observed in the SE-CARS image.

In Fig. 12(a), we visualized several polystyrene structures of various shapes and thicknesses, obtained by melting 3 μm polystyrene spheres on the gold. The image is recorded at 2845 cm^{-1}, near the CH_2 symmetric stretching mode of polystyrene. The difference between spherical scatterers and more

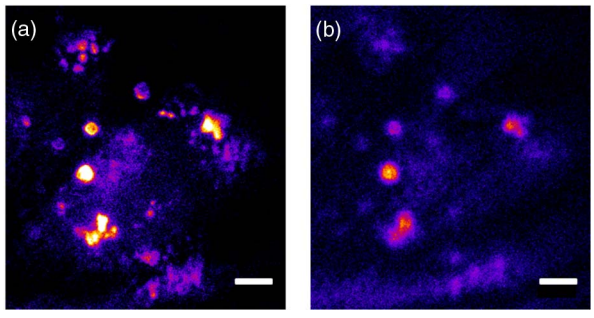

Fig. 11. Cholesteryl oleate lipid droplets in water. (a) An SE-CARS image at 2845 cm^{-1}. (b) An TPEF image obtained by blocking the Stokes beam. The scale bars are 20 μm.

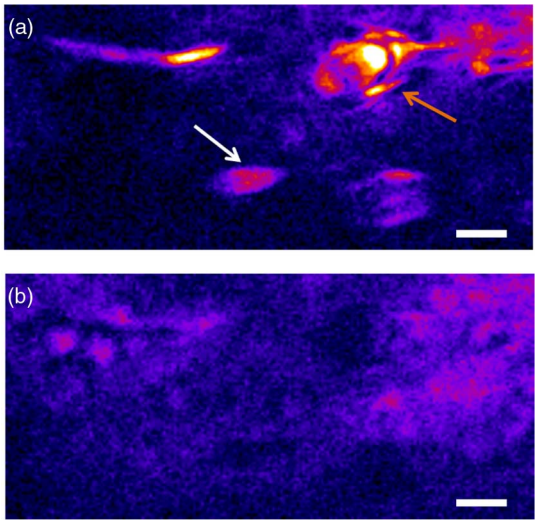

Fig. 12. Polystyrene structures in water. (a) An SE-CARS image at 2845 cm^{-1}. (b) An SE-CARS image at 2960 cm^{-1}. The scale bars are 5 μm.

planar shapes is apparent. Spherical beads, indicated by the white arrow, tend to leave small streaking jets that move away from the sample in the direction of SPP propagation. This appears to be consistent with the small penetration depth of the SPP field in z which excites only a small portion of the sphere's bottom. The orange arrow points to a thin and flat layer of polystyrene that provides another good example of flaring. The coherent nature of the radiation is evident from the interference that can be distinguished in the flares. Note that a weak signal can be seen in areas where no structures are present. This signal results from the non-resonant SE-CARS signal from the medium (water). This is made clearer in Fig. 12(b), where the same structures are imaged at 2960 cm^{-1}, a vibrational energy at which the resonant SE-CARS signal interferes destructively with the non-resonant signal from water. The polystyrene structures now appear dark against a background of predominantly non-resonant SE-CARS signal.

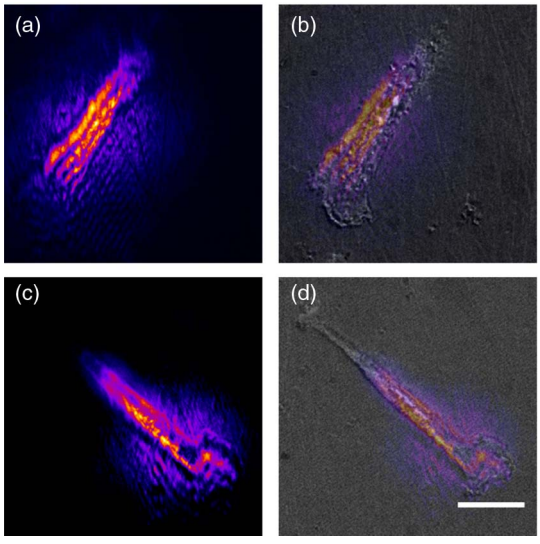

Fig. 13. MCF7 breast cancer cells. (a, c) A CARS image at 2845 cm^{-1}. (b, d) An overlay of the CARS and transmission images. The scale bar is 20 μm.

Finally, in Fig. 13, we provide images of cells adhered to the gold surface. To improve the image contrast, we have dried the cells in air, resulting in a higher concentration of cellular material close to the surface. Under these conditions, strong SE-CARS signals are obtained, which co-localize with the transmission image of the cells. These signals are reduced when the Raman shift is tuned off resonance. Although this example is not representative of typical cellular imaging conditions, it does illustrate that (vibrationally resonant) SE-CARS signals can be generated from cellular materials. At the same time, improvements are needed to bring cells in aqueous media into sharper view.

4. DISCUSSION

In this work, we discussed the imaging properties of wide-field SE-CARS in detail. Although the SPP-based CARS microscope shares its spectroscopic sensitivity with conventional CARS microscopy, its imaging properties are radically different. Whereas in regular CARS imaging, the phase-matched coherent radiation from molecules in the focal volume is integrated on a single pixel, far-field detector [22], in wide-field SE-CARS the radiation is collected on a detector array in directions that are mutual to the propagation direction of the SPP excitation fields. Therefore, image features seen in SE-CARS imaging cannot be directly compared with features known from conventional CARS microscopy. Rather, in terms of excitation and detection geometry, the SPP-based CARS microscope has more in common with surface plasmon resonance imaging (SPRi) [40–42] and surface plasmon coupled emission microscopy (SPCEM) [43–45]. Similar to SPRi and SPCEM, the radiation from the sample is strongly influenced by the metal film.

The signals detected in the wide-field SE-CARS microscope originate from different mechanisms. First, there are incoherent emission contributions. These contributions come from excited fluorophores that might be in the sample, in addition to the TPEF from the gold layer itself. These fluorescence contributions always manifest themselves as a ring-like radiation pattern in the BFP, irrespective of the distribution of the fluorosphores in the sample plane.

Second, there are coherent radiation contributions in the SE-CARS microscope. The coherent radiation originates from driven dipoles in the upper half-space, derived from a vibrational or electronic CARS process, thus producing radiation at ω_{as}. Importantly, the radiation pattern depends on the distance of the dipole oscillator from the surface. For the closest dipoles, SPP waves at ω_{as} are excited and coupling is at the plasmon coupling angle, resulting in a ring-like pattern in the BFP. Constructive interference between the radiation from different dipoles produces stronger signals and preferred propagating of the excited SPP waves in the phase-matched direction, leading to flares and streaks in the SE-CARS image. The SPP contribution is suppressed for dipole radiators farther away from the surface, thus producing CARS images that are devoid of streaks. Generally, we observe streaks for very thin samples such as phospholipid bilayers, whereas flare-free images are

observed for thicker samples such as droplets of neutral lipids. Hence, our dipole-based model explains the differences in the appearance of the images depending on the object being imaged.

Like the conventional CARS microscope, the SE-CARS instrument is capable of generating images with vibrational contrast. However, the SE-CARS images are affected by a strongerTPEF background, in addition to the appearance of streaks and flares due to SPP propagation. These features affect the interpretation of the SE-CARS images, which are generally more difficult to interpret than the images generated in a point-scanning CARS microscope. A better understanding of the origins of SE-CARS image features, such as presented here, can help guide the image interpretation and thus improve the utility of the SE-CARS microscope.

Despite the more complex image properties of the wide-field SE-CARS microscope, the efficiency of CARS signal generation is many orders of magnitude higher than in a point-scanning microscope. For instance, assuming an image acquisition time of 1 s, the integrated signal level for a GUV bilayer is about the same as that seen in the SE-CARS and the conventional CARS microscope. At the same time, the incident pulse energy per μm^2 in the SE-CARS microscope is more than four orders of magnitude lower [20]. Part of this higher efficiency is due to the fact that the pixel dwell time is much higher in the wide-field detection, amounting to 1 s per pixel for SE-CARS versus ~1 μs per pixel for the point-scanning microscope. Even so, bringing down the pulse energy in a regular CARS microscope to ~70 $fJ/\mu m^2$, as is the case in the SE-CARS measurement, and integrating for 1 s would still yield signals that are lower by more than 10^7. This enormous increase in SE-CARS signal generation efficiency is due to the surface-enhancement effect facilitated by the flat gold film. The effective field enhancement provided by the surface is much smaller than what is common for the "hotspots" in SERS, typically less than a factor of 10. Yet, the nonlinearity of the CARS process combined with the enhancement of the radiative rate at ω_{as} afforded by the film still produces an effective signal enhancement of more than seven orders of magnitude. Unlike in SERS, this enhancement is not localized to specific spots, but is *uniform* across the entire field of view instead. In effect, the surface enhancement in wide-field SE-CARS allows the amplification of an entire image with a factor of ~10^7. The latter is the true merit of this type of microscope.

5. CONCLUSION

In this work, we have experimentally and theoretically analyzed the imaging properties of the wide-field SE-CARS microscope. Using a dipole model to describe the sample, we have found that for thin samples such as lipid bilayers, SPP waves are efficiently excited at the anti-Stokes frequency, producing strong CARS signals with incident pulse energies as low as 70 $fJ/\mu m^2$. However, the coherent SPP waves at the signal frequency give rise to flares and interfering streaks in the image. For thicker samples, such as lipid droplets, the SPP contribution is relatively small, producing SE-CARS images free of propagation artifacts. The use of a thin gold film gives rise to a signal enhancement of more than seven orders of magnitude relative to CARS generation with freely propagating light. With a better understanding of the imaging properties of the wide-field SE-CARS microscope, this imaging method may prove useful for imaging and sensing applications in which low light levels per unit area are required.

APPENDIX A

The far-field Green's function that relates a wave emitted at point $\mathbf{r}'$ in the upper half-space through a layered medium to a far-field point $\mathbf{r}$ in the lower half-space, is given in the angular spectrum representation as [21]

$$\overline{G}(\mathbf{r},\mathbf{r}') = \frac{e^{ik_3(r+\delta z/r)}e^{\left\{-ik_1\left(\frac{x'x}{r}+\frac{y'y}{r}-z'\sqrt{1-(n_3/n_1)^2(\rho/r)^2}\right)\right\}}}{4\pi r}\times\overline{\mathbf{M}}, \tag{A1}$$

where the matrix $\overline{\mathbf{M}}$ is given as

$$\overline{\mathbf{M}} = \begin{bmatrix} \frac{x^2}{\rho^2}\frac{z^2}{r^2}\Phi^{(2)}+\frac{y^2}{\rho^2}\Phi^{(3)} & \frac{xy}{\rho^2}\frac{z^2}{r^2}\Phi^{(2)}-\frac{xy}{\rho^2}\Phi^{(3)} & \frac{-xz}{r^2}\Phi^{(1)} \\ \frac{xy}{\rho^2}\frac{z^2}{r^2}\Phi^{(2)}-\frac{xy}{\rho^2}\Phi^{(3)} & \frac{y^2}{\rho^2}\frac{z^2}{r^2}\Phi^{(2)}+\frac{x^2}{\rho^2}\Phi^{(3)} & \frac{-yz}{r^2}\Phi^{(1)} \\ \frac{-xz}{r^2}\Phi^{(2)} & \frac{-yz}{r^2}\Phi^{(2)} & \left(1-\frac{z^2}{r^2}\right)\Phi^{(1)} \end{bmatrix}. \tag{A2}$$

Here, $\rho=\sqrt{x^2+y^2}$ and the functions $\Phi_3^{(i)}$ with $i=(1,2,3)$ are written as

$$\Phi^{(1)} = t^P(k_\rho)\frac{n_3}{n_1}\frac{k_3 z/r}{\sqrt{k_1^2-k_\rho^2}}, \tag{A3}$$

$$\Phi^{(2)} = -t^P(k_\rho)\frac{n_3}{n_1}, \tag{A4}$$

$$\Phi^{(3)} = t^S(k_\rho)\frac{k_3 z/r}{\sqrt{k_1^2-k_\rho^2}}, \tag{A5}$$

where $k_\rho = k_3\rho/r$, and t^P and t^S are the generalized Fresnel coefficients for P and S polarized light, respectively. The generalized transmission and reflection coefficient for the water-gold-glass stratified medium considered here are

$$t^{(P,S)} = \frac{t_{1,2}^{(P,S)}t_{2,3}^{(P,S)}e^{(ik_{2z}d)}}{1+r_{1,2}^{(P,S)}r_{2,3}^{(P,S)}e^{(2ik_{2z}d)}}, \tag{A6}$$

$$r^{(P,S)} = \frac{r_{1,2}^{(P,S)}+r_{2,3}^{(P,S)}e^{(2ik_{2z}d)}}{1+r_{1,2}^{(P,S)}r_{2,3}^{(P,S)}e^{(2ik_{2z}d)}}, \tag{A7}$$

where d is the thickness of the gold layer. The expressions in Eqs. (A6) and (A7) depend on the Fresnel coefficients at each of the interfaces as

$$r_{i,j}^S(k_\rho) = \frac{\mu_j k_{z_i}-\mu_i k_{z_j}}{\mu_j k_{z_i}+\mu_i k_{z_j}}, \tag{A8}$$

$$r_{i,j}^P(k_\rho) = \frac{\varepsilon_j k_{z_i}-\varepsilon_i k_{z_j}}{\varepsilon_j k_{z_i}+\varepsilon_i k_{z_j}}, \tag{A9}$$

and

$$t_{i,j}^{S}(k_\rho) = \frac{2\mu_j k_{z_i}}{\mu_j k_{z_i} + \mu_i k_{z_j}}, \tag{A10}$$

$$t_{i,j}^{P}(k_\rho) = \frac{2\varepsilon_j k_{z_i}}{\varepsilon_j k_{z_i} + \varepsilon_i k_{z_j}} \sqrt{\frac{\mu_j \varepsilon_i}{\mu_i \varepsilon_j}}. \tag{A11}$$

Funding. National Science Foundation (NSF) (DBI-1454885, CHE-1414466).

REFERENCES

1. D. L. Jeanmaire and R. P. V. Duyne, "Surface Raman spectroelectrochemistry," J. Electroanal. Chem. Interfacial Electrochem. **84**, 1–20 (1977).
2. G. C. Schatz, "Theoretical studies of surface enhanced Raman scattering," Acc. Chem. Res. **17**, 370–376 (1984).
3. S. Nie and S. R. Emory, "Probing single molecules and single nanoparticles by surface-enhanced Raman scattering," Science **275**, 1102–1106 (1997).
4. K. Kneipp, Y. Wang, H. Kneipp, L. T. Perelman, I. Itzkan, R. R. Dasari, and M. S. Feld, "Single molecule detection using surface-enhanced Raman scattering (SERS)," Phys. Rev. Lett. **78**, 1667–1670 (1997).
5. J. A. Dieringer, R. B. Lettan, K. A. Scheidt, and R. P. Van Duyne, "A frequency domain existence proof of single-molecule surface-enhanced Raman spectroscopy," J. Am. Chem. Soc. **129**, 16249–16256 (2007).
6. C. Steuwe, C. F. Kaminski, J. J. Baumberg, and S. Mahajan, "Surface enhanced coherent anti-Stokes Raman scattering on nanostructured gold surfaces," Nano Lett. **11**, 5339–5343 (2011).
7. J. Giergiel, C. E. Reed, J. C. Hemminger, and S. Ushioda, "Surface plasmon polariton enhancement of Raman scattering in a Kretschmann geometry," J. Phys. Chem. **92**, 5357–5365 (1988).
8. S. A. Meyer, E. C. Le Ru, and P. G. Etchegoin, "Combining surface plasmon resonance (SPR) spectroscopy with surface-enhanced Raman scattering (SERS)," Anal. Chem. **83**, 2337–2344 (2011).
9. S. A. Meyer, B. Auguié, E. C. Le Ru, and P. G. Etchegoin, "Combined SPR and SERS microscopy in the Kretschmann configuration," J. Phys. Chem. A **116**, 1000–1007 (2012).
10. H. Li, S. Xu, Y. Liu, Y. Gu, and W. Xu, "Directional emission of surface-enhanced Raman scattering based on a planar-film plasmonic antenna," Thin Solid Films **520**, 6001–6006 (2012).
11. H.-W. Yoo, L. J. Richter, H.-T. Jung, and C. A. Michaels, "Surface plasmon polariton Raman microscopy," Vib. Spectrosc. **60**, 85–91 (2012).
12. D. Zerulla, G. Isfort, M. Kölbach, A. Otto, and K. Schierbaum, "Sensing molecular properties by ATR-SPP Raman spectroscopy on electrochemically structured sensor chips," Electrochim. Acta **48**, 2943–2947 (2003).
13. C. L. Evans, E. O. Potma, M. Puoris'haag, D. Côté, C. P. Lin, and X. S. Xie, "Chemical imaging of tissue in vivo with video-rate coherent anti-Stokes Raman scattering microscopy," Proc. Natl. Acad. Sci. USA **102**, 16807–16812 (2005).
14. B. G. Saar, C. W. Freudiger, J. Reichman, C. M. Stanley, G. R. Holtom, and X. S. Xie, "Video-rate molecular imaging in vivo with stimulated Raman scattering," Science **330**, 1368–1370 (2010).
15. J.-X. Cheng and X. S. Xie, *Coherent Raman Scattering Microscopy* (CRC Press, 2013).
16. C. K. Chen, A. R. B. de Castro, Y. R. Shen, and F. DeMartini, "Surface coherent anti-Stokes Raman spectroscopy," Phys. Rev. Lett. **43**, 946–949 (1979).
17. Y. Zhang, Y.-R. Zhen, O. Neumann, J. K. Day, P. Nordlander, and N. J. Halas, "Coherent anti-Stokes Raman scattering with single-molecule sensitivity using a plasmonic Fano resonance," Nat. Commun. **5**, 4424 (2014).
18. S. Yampolsky, D. A. Fishman, S. Dey, E. Hulkko, M. Banik, E. O. Potma, and V. A. Apkarian, "Seeing a single molecule vibrate through time-resolved coherent anti-Stokes Raman scattering," Nat. Photonics **8**, 650–656 (2014).
19. K. T. Crampton, A. Zeytunyan, A. S. Fast, F. T. Ladani, A. Alfonso-Garcia, M. Banik, S. Yampolsky, D. A. Fishman, E. O. Potma, and V. A. Apkarian, "Ultrafast coherent Raman scattering at plasmonic nanojunctions," J. Phys. Chem. C **120**, 20943–20953 (2016).
20. A. Fast, J. P. Kenison, C. D. Syme, and E. O. Potma, "Surface-enhanced coherent anti-Stokes Raman imaging of lipids," Appl. Opt. **55**, 5994–6000 (2016).
21. L. Novotny and B. Hecht, *Principles of Nano-Optics* (Cambridge University, 2012).
22. J.-X. Cheng, A. Volkmer, and X. S. Xie, "Theoretical and experimental characterization of coherent anti-Stokes Raman scattering microscopy," J. Opt. Soc. Am. B **19**, 1363–1375 (2002).
23. V. V. Krishnamachari and E. O. Potma, "Focus-engineered coherent anti-Stokes Raman scattering microscopy: a numerical investigation," J. Opt. Soc. Am. A **24**, 1138–1147 (2007).
24. P. B. Johnson and R.-W. Christy, "Optical constants of the noble metals," Phys. Rev. B **6**, 4370–4379 (1972).
25. D. Axelrod, T. P. Burghardt, and N. L. Thompson, "Total internal reflection fluorescence," Annu. Rev. Biophys. Bioeng. **13**, 247–268 (1984).
26. A. Trache and G. A. Meininger, *Total Internal Reflection Fluorescence (TIRF) Microscopy* (Wiley, 2005).
27. R.-Y. He, Y.-D. Su, K.-C. Cho, C.-Y. Lin, N.-S. Chang, C.-H. Chang, and S.-J. Chen, "Surface plasmon-enhanced two-photon fluorescence microscopy for live cell membrane imaging," Opt. Express **17**, 5987–5997 (2009).
28. C.-Y. Lin, K.-C. Chiu, C.-Y. Chang, S.-H. Chang, T.-F. Guo, and S.-J. Chen, "Surface plasmon-enhanced and quenched two-photon excited fluorescence," Opt. Express **18**, 12807–12817 (2010).
29. I. Gryczynski, J. Malicka, Z. Gryczynski, and J. R. Lakowicz, "Surface plasmon-coupled emission with gold films," J. Phys. Chem. B **108**, 12568–12574 (2004).
30. G. T. Boyd, Z. H. Lu, and Y. R. Shen, "Photoinduced luminescence from the noble metals and its enhancement on roughened surfaces," Phys. Rev. B **33**, 7923–7936 (1986).
31. J.-X. Cheng, A. Volkmer, L. D. Book, and X. S. Xie, "Multiplex coherent anti-Stokes Raman scattering microspectroscopy and study of lipid vesicles," J. Phys. Chem. B **106**, 8493–8498 (2002).
32. E. O. Potma and X. S. Xie, "Detection of single lipid bilayers with coherent anti-Stokes Raman scattering (CARS) microscopy," J. Raman Spectrosc. **34**, 642–650 (2003).
33. M. A. Lieb, J. M. Zavislan, and L. Novotny, "Single-molecule orientations determined by direct emission pattern imaging," J. Opt. Soc. Am. B **21**, 1210–1215 (2004).
34. T. Shegai, V. D. Miljkovic, K. Bao, H. Xu, P. Nordlander, P. Johansson, and M. Kall, "Unidirectional broadband light emission from supported plasmonic nanowires," Nano Lett. **11**, 706–711 (2011).
35. L. Novotny, "Allowed and forbidden light in near-field optics. I. A single dipolar light source," J. Opt. Soc. Am. A **14**, 91–104 (1997).
36. B. Hecht, H. Bielefeldt, L. Novotny, Y. Inouye, and D. Pohl, "Local excitation, scattering, and interference of surface plasmons," Phys. Rev. Lett. **77**, 1889–1892 (1996).
37. I. I. Smolyaninov, D. L. Mazzoni, J. Mait, and C. C. Davis, "Experimental study of surface-plasmon scattering by individual surface defects," Phys. Rev. B **56**, 1601–1611 (1997).
38. A. Drezet and C. Genet, "Imaging surface plasmons: from leaky waves to far-field radiation," Phys. Rev. Lett. **110**, 213901 (2013).
39. J. J. Foley IV, H. Harutyunyan, D. Rosenmann, R. Divan, G. P. Wiederrecht, and S. K. Gray, "When are surface plasmon polaritons excited in the Kretschmann-Raether configuration?" Sci. Rep. **5**, 9929 (2015).
40. C. Boozer, G. Kim, S. Cong, H. Guan, and T. Londergan, "Looking towards label-free biomolecular interaction analysis in a high-throughput format: a review of new surface plasmon resonance technologies," Curr. Opin. Biotechnol. **17**, 400–405 (2006).
41. B. Huang, F. Yu, and R. N. Zare, "Surface plasmon resonance imaging using a high numerical aperture microscope objective," Anal. Chem. **79**, 2979–2983 (2007).
42. A. R. Halpern, J. B. Wood, Y. Wang, and R. M. Corn, "Single-nanoparticle near-infrared surface plasmon resonance microscopy

for real-time measurements of DNA hybridization adsorption," ACS Nano **8**, 1022–1030 (2014).
43. J. R. Lakowicz, J. Malicka, I. Gryczynski, and Z. Gryczynski, "Directional surface plasmon-coupled emission: a new method for high sensitivity detection," Biochem. Biophys. Res. Commun. **307**, 435–439 (2003).
44. F. D. Stefani, K. Vasilev, N. Bocchio, N. Stoyanova, and M. Kreiter, "Surface-plasmon-mediated single-molecule fluorescence through a thin metallic film," Phys. Rev. Lett. **94**, 023005 (2005).
45. J. Borejdo, N. Calander, Z. Gryczynski, and I. Gryczynski, "Fluorescence correlation spectroscopy in surface plasmon coupled emission microscope," Opt. Express **14**, 7878–7888 (2006).

169.234.5.113 {ts '2017-09-08 18:04:17'}